Solar RRL
www.solar-rrl.com

Crack-Free Monolayer Graphene Interlayer for Improving Perovskite Crystallinity and Energy Level Alignment in Efficient Inverted Perovskite Solar Cells

*Ruiyuan Hu, Yonggui Sun, Lutao Li, Taomiao Wang, Hiroyuki Kanda, Cheng Liu, Yi Yang, Shiqi Huang, Abdullah M. Asiri, Liang Chu, Xing'ao Li, Kumar Varoon Agrawal, and Mohammad Khaja Nazeeruddin**

Inverted planar perovskite solar cells (PSCs) have intrigued great promise in negative hysteresis, simple fabrication process, and flexible substrate implementation, in which the shared hole transport materiel is NiO_x. However, the low-temperature solution processing of the NiO_x film is usually accompanied by defect formation, which deteriorates the perovskite quality and device performance. Meanwhile, the energy-level offset between the NiO_x and perovskite films is relatively large, limiting the interfacial charge transport. To suppress those setbacks, a defect-free monolayer graphene sheet is transferred onto the NiO_x film surface as a template for van der Waals epitaxial growth of perovskite films for the first time, leading to enhancing crystallinity with a large grain size of perovskite layer, 0.20 eV energy level offset drop, and accelerating charge transfer for the devices. Finally, the power conversion efficiency of 19.21% without hysteresis is achieved, exceeding 18.35% of the control device.

1. Introduction

Halide perovskite materials have exceptional photoelectric properties, such as high absorption coefficient, appropriate direct bandgap, long carrier diffusion length, and low exciton binding energy.[1,2] Typically, perovskite solar cells (PSCs) have boosted certified power conversion efficiency (PCE) up to 25.7%,[3] being rendered comparable with current commercial solar cells. In PSCs, perovskite film is sandwiched between the electron-transport layer (ETL) and hole-transport layer (HTL).[4] In perovskite film, the electron–hole pairs are generated after capturing photons, then separated and transported into the ETL and HTL, respectively, and finally collected through both two electrodes as photocurrent.[5] In the aforementioned working process, the perovskite crystallinity and energy level alignment are critical to the photovoltaic parameters of PSCs, such as open-circuit voltage (V_{OC}), and short-circuit current (J_{SC}), and fill factor (FF).

According to the device architectures, the PSCs can be categorized in planar and mesoporous types on whether using the mesoporous scaffolds. The highly efficient PSCs are usually achieved on metal-oxide-based mesoporous architecture.[6] However, the mesoporous scaffolds are commonly fabricated with requiring high-temperature annealing, which increases the cost of production and hinders the progress of flexible modules. While the inverted planar PSCs reveal great promise in negative hysteresis, simple fabrication process, and flexible substrate implementation.[7] In the inverted planar device, the HTL, besides being a major role in hole extraction, serves as the landing surface for the growing perovskite layer. Thus, the perovskite crystallinity is crucially affected by the surface of HTL. Meanwhile, the less energy level offset at the HTL and perovskite interface is essential for reducing the loss of V_{OC} and enhancing charge transfer.

In inverted planar PSCs, poly(3,4-ethylenedioxythiophene): poly(styrenesulfonate) (PEDOT:PSS), poly(triarylamine) (PTAA), and nickel oxide (NiO_x) are the most frequently materials of HTL.[8] Though PEDOT:PSS was first applied as HTL in inverted PSCs, its natural hygroscopicity and acidity induce instability and give rise to low performance. In addition, the highest occupied

R. Hu, Y. Sun, L. Li, T. Wang, L. Chu, X. Li
New Energy Technology Engineering Laboratory of Jiangsu Province
School of Science
School of Materials Science and Engineering
Nanjing University of Posts and Telecommunications (NJUPT)
Nanjing 210023, China

H. Kanda, C. Liu, Y. Yang, M. K. Nazeeruddin
Group for Molecular Engineering of Functional Materials
Laboratory of Advanced Separations
École Polytechnique Fédérale de Lausanne (EPFL)
1951 Sion, Switzerland
E-mail: mdkhaja.nazeeruddin@epfl.ch

S. Huang
Laboratory of Advanced Separations (LAS)
École Polytechnique Fédérale de Lausanne (EPFL)
1951 Sion, Switzerland

A. M. Asiri
Center of Excellence for Advanced Materials Research (CEAMR)
King Abdulaziz University
Jeddah 21589, Saudi Arabia

The ORCID identification number(s) for the author(s) of this article can be found under https://doi.org/10.1002/solr.202200484.

DOI: 10.1002/solr.202200484

molecular orbital (HOMO) level of PEDOT:PSS (5.0 eV) cannot match well with the valence band maximum (VBM) of the perovskite layers, which strongly limits the theoretical *Voc*. Compared with the PEDOT:PSS, PTAA HTL in an inverted device has better stability and hole transferability, but the material synthesis needs a more complex process and high cost, limiting the large scale utilization.[9] The inorganic NiO_x HTL has attracted much attention due to its low-cost, good transparency in the visible and infrared region, good hole transport ability, and excellent stability. The record PCE is over 22% of the $MAPbI_3$-based inverted PSCs with NiO_x HTL.[10–12]

To date, the NiO_x HTL in inverted PSC has been prepared by various methods, such as magnetron sputtering, electron beam deposition, pulsed laser deposition, and solution process.[13] Among them, the solution process to fabricate NiO_x HTL has been considered a promising approach due to its simple fabrication, low cost, and high yield. However, the solution-processed NiO_x HTL is subjected to the natural randomly distributed defects and intrinsic conductivity.[14] In serious cases, the natural defects influence the perovskite nucleation and crystallinity randomly. Meanwhile, the HOMO level of NiO_x HTL is 5.3 eV, resulting in a large offset of energy level in $MAPbI_3$-based inverted PSCs.[15] Therefore, interface engineering has been considered an effective way for the solution-processed NiO_x HTL to achieve higher efficiency of PSCs, which can improve the conductivity, modify the energy level, and reduce the surface defects for perovskite crystallization.[16–18]

Monolayer graphene (MLG) is a strictly 2D crystal of carbon atoms that exhibits excellent conductivity, extraordinary optical transmittance, high flexibility, and stability.[19,20] In addition, high-quality crack-free MLG has a super-clean surface and homogeneousness with a six-member ring structure composed of carbon atoms.[21] A prior study indicated that MLG induces the crystallization of P3HT films, where the particular crystalline mosaic with π–π stacking oriented homogeneously at various angles inside the film favors the creation of a continuous pathway of interconnected crystallites for charge transport.[22] Meanwhile, due to the large special surface area and highly delocalized electrons, MLG can regulate energy levels at the interface and produce efficient charge transfer when in contact with a semiconductor.[23]

In this article, a large-area sheet of crack-free MLG was transferred onto the surface of NiO_x film for enhancement of inverted planar PSCs. The defect-free ultra-clean MLG was conducted as a template for van der Waals epitaxial growth of perovskite films by solution process for the first time. The crystallinity of perovskite film was enhanced, and grain size increased about three times. An obvious drop of 0.20 eV of energy level offset was achieved for the NiO_x-based hole transport layer, which accelerated the charge transport and extraction for the devices. In the device structure of fluorine-doped tin oxide (FTO)/NiO_x/MLG/$MAPbI_3$/PCB61M/PCP/Ag, PCE of 19.21% without hysteresis was achieved with the improvement in parameters of Voc (1.093 V), Jsc (22.6 mA cm^{-2}), and FF (77.8%), exceeding 18.35% (PCE) of the control device.

2. Results and Discussions

2.1. Crack-Free MLG Transfer on NiO_x

The schematic diagram of transferring crack-free MLG on NiO_x film is illustrated in **Figure 1**a. The MLG-modified NiO_x film is fabricated as follows: NiO_x nanoparticle aqueous dispersion is spin-coated on FTO conductive glass. MLG is synthesized on Cu foil by chemical vapor deposition (CVD), then the MLG is crack freely transferred onto NiO_x film with the sacrificial mechanically reinforcing polymer film, which is low-temperature processed.[24] The top-view scanning electron microscope (SEM) image of MLG-modified NiO_x film verified the crack-freely transfer of MLG in Figure 1b. Meanwhile, the Raman spectrum also confirmed the MLG-modified NiO_x film, shown in Figure 1c. In the Raman spectrum of NiO_x/MLG film, the peak of the G-band is the characteristic peak of graphene, resulting from the in-plane vibration of sp^2 carbon atoms.[25] The symmetric peak of the 2D-band is sharp with full width at half-maximum about 35 cm^{-1}, indicating the monolayer graphene. The inconspicuous peak of the D-band suggests few defects in the graphene layer. Besides, the peak located at 1085.2 cm^{-1} is assigned to 2 longitudinal optical (2LO) phonon modes of NiO_x.[26] The morphology is investigated via SEM. Figure S1a and S1b, Supporting Information, exhibits uniform and smooth surfaces of both NiO_x and NiO_x/MLG films, which is considered to contribute to full coverage and crystallization of the $MAPbI_3$ film.[27] In addition, after covering MLG on NiO_x film, the decreased roughness will be beneficial to fabricating perovskite film in high quality (shown in Figure S1c–f, Supporting Information).

2.1.1. $MAPbI_3$ Crystallization Modification by MLG

In inverted PSC, the NiO_x layer is in front of perovskite film under illumination. Therefore, the transparency of NiO_x should be high to ensure $MAPbI_3$ absorbs the light and generates carriers. Comparing the UV–vis absorption and transmittance of NiO_x and NiO_x/MLG film, the NiO_x/MLG film displays a slightly stronger absorption than NiO_x film (**Figure 2**a). However, given that MLG is an atomic layer with high optical transmittance, it would not influence the substrate transparency significantly, which is demonstrated in the transmittance spectra of NiO_x and NiO_x/MLG films (Figure 2b). At the same time, the UV–vis absorption of $MAPbI_3$ is slightly enhanced after MLG-modified NiO_x as substrate (see Figure 2c), which also indicates a higher quality of $MAPbI_3$ obtained on NiO_x/MLG.

In the meanwhile, the MLG modification has changed certain properties of NiO_x film. The typical X-ray diffraction (XRD) patterns of $MAPbI_3$ on NiO_x and NiO_x/MLG substrate are presented in **Figure 3**a. The main strong peaks of both films at 14.2°, 28.5°, and 32.0° correspond to the (110), (220), and (310) planes, respectively,[28] which are indexed to the perovskite structure. All the peaks are attributed to $MAPbI_3$ and FTO, suggesting that a pure phase of $MAPbI_3$ is obtained. The crystallization of $MAPbI_3$ is improved when deposited on NiO_x/MLG, as it shows stronger diffraction peaks than those on NiO_x. It is essential to achieve high photovoltaic performance with high-quality perovskite films. Figure 3b,c displays surface SEM images of NiO_x-$MAPbI_3$ and NiO_x/MLG-$MAPbI_3$, which show the $MAPbI_3$ with dense, smooth, and pinhole-free. By comparison, the grain size of $MAPbI_3$ on NiO_x/MLG is more uniform and slightly larger than that on NiO_x, which agrees with the result of XRD that the MLG modified NiO_x improves the crystallization of $MAPbI_3$.

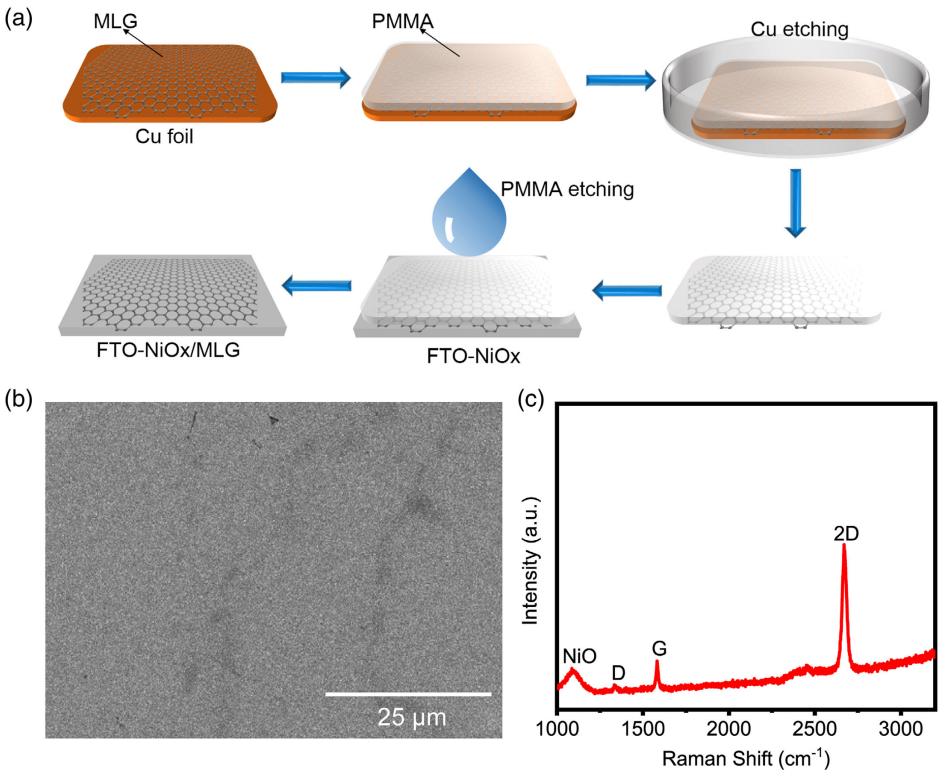

Figure 1. a) Schematic diagram of the monolayer graphene (MLG) crack-free transfer to fluorine-doped tin oxide (FTO)-NiO_x substrate; b) top-view scanning electron microscope (SEM) image of FTO-NiO_x/MLG; c) Raman spectrum of NiO_x/MLG film.

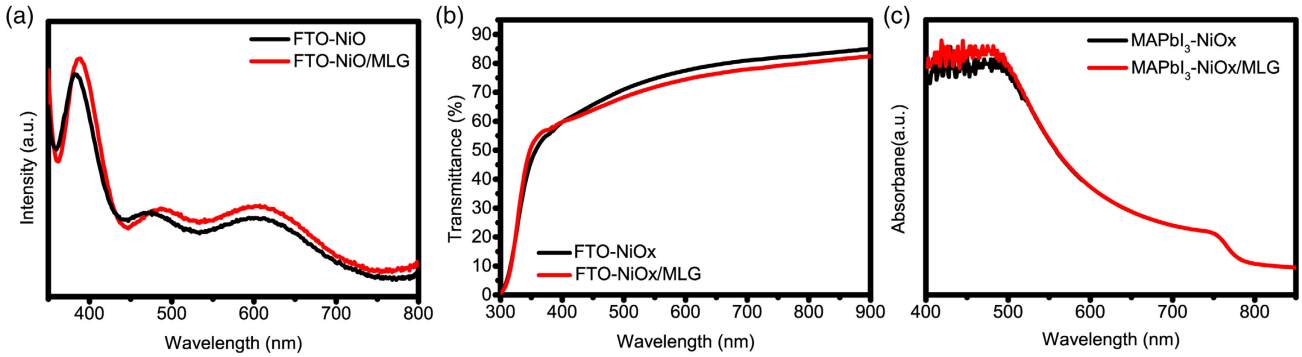

Figure 2. a) UV–vis absorption and b) transmittance spectra of NiO_x and NiO_x/MLG films on FTO; c) UV–vis absorption spectra of $MAPbI_3$ films on NiO_x and NiO_x/MLG.

2.1.2. Hole Transportation Improvement by MLG

To inspect the effect of MLG modification on the energy level of NiO_x film, ultraviolet photoelectron spectroscopy (UPS) is carried out. The details that calculate the work function (WF) and valence band maximum (E_{VBM}) are illustrated in **Figure 4**a for NiO_x and 4b for NiOx/MLG. Briefly, the energy of the ultraviolet source (Helium Iα) is 21.22 eV (as the wavelength of Helium Iα is 58.13 nm).[29] WF is calculated via 21.22 minus the high binding energy cutoff. Thus, $WF_{NiOx} = 4.05$ eV and $WF_{NiOx/MLG} = 4.42$ eV. For E_{VBM}, it is obtained by totaling WF and the low binding energy cut-off, which $E_{VBM,\ NiOx} = 5.16$ eV and $E_{VBM,\ NiOx/MLG} = 5.36$ eV. The results of UPS demonstrate that with the modification of MLG, the WF and E_{VBM} of HTL are increased that closer to the E_{VBM} of perovskite. The shift of E_{VBM} indicates that it improves hole extraction and better band alignment between HTL and $MAPbI_3$ valence band, which will discuss below details. The hole extraction of HTL is the key factor to affect the photovoltaic performance of PSCs. Steady-state photoluminescence (PL) measurement is usually implemented to evaluate the hole extraction ability of the thin films. Figure 4c illustrates the PL spectra of $MAPbI_3$ on different substrates with an excitation wavelength 500 nm irradiated from the $MAPbI_3$ film side. On

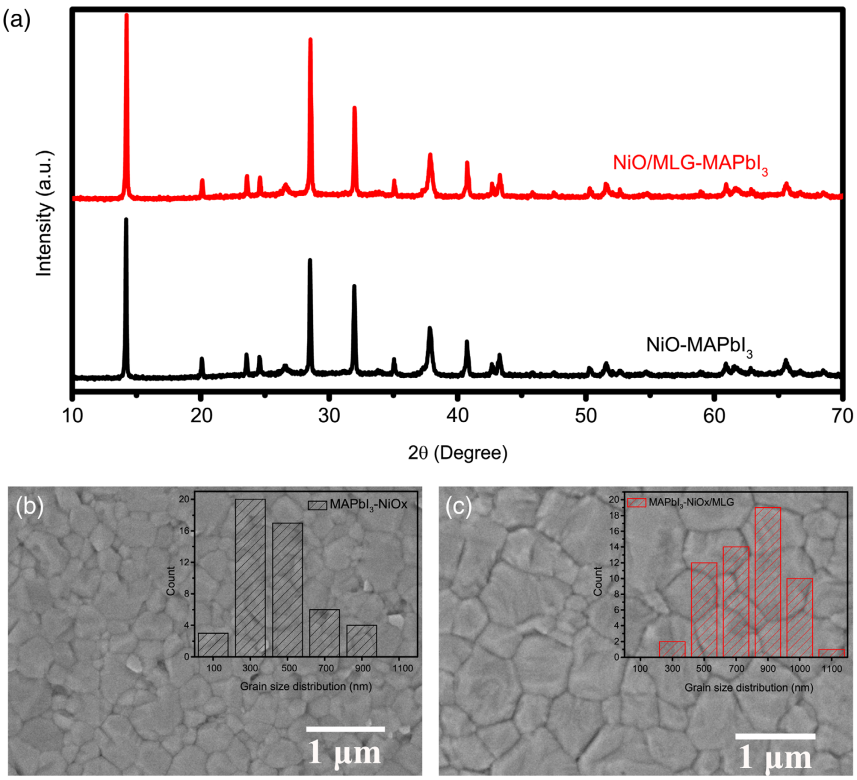

Figure 3. a) Typical X-ray diffraction (XRD) pattern of the $MAPbI_3$ films on NiO_x and NiO_x/MLG; Top-view SEM images and of $MAPbI_3$ films on: b) NiO_x and c) NiO_x/MLG.

the bare glass, $MAPbI_3$ appears to have a strong luminescence peak at ≈775 nm, because of serious carrier recombination. It is well-known that surface modification is a facile and effective way to enhance the contact and transport of carries between perovskite and ETL/HTL. To further investigate the hole transfer dynamics between $MAPbI_3$ and HTL, PL spectra of $MAPbI_3$ on NiO_x and NiO_x/MLG are compared. First, the peak intensities decrease obviously after importing HTL, implying the improvement of the extracting charge carriers. Then, the peak intensity of $MAPbI_3$ on NiO_x/MLG is slightly lower than that of $MAPbI_3$ on NiO_x, which can confirm that NiO_x/MLG extract holes more efficiently. From the corresponding time-resolved PL (TRPL) spectra of $MAPbI_3$ on HTL shown in Figure 4d, the average fitting carrier life-time (τ_{avg}) for the sample based on NiO_x is 35 ns and for that based on NiO_x/MLG is 20 ns, which listed the fitting parameters in Table S1, Supporting Information. The slightly shorter τ_{avg} demonstrates the improved hole extraction property, which can lead to higher Voc in PSCs. To further explore the hole extraction and transport mechanism, we draw the schematic diagram of $MAPbI_3$ and HTL interface under illumination in Figure 4e. The HTL plays the role of an energy barrier to inhibit the recombination of holes. Hence, the band alignment for HTL and $MAPbI_3$ is essential for the photovoltaic performance.[30] The energy barrier for hole transfer from $MAPbI_3$ to HTL is eliminated, because of the reduced valence band offset from 0.24 to 0.04 eV. Consequently, the carrier recombination is suppressed, and the hole extraction is enhanced, which improves device Voc.[31] When the carriers transfer from $MAPbI_3$ to HTL, they could lose part of free energy owing to the misaligned energy band, which would cause additional V_{oc} loss. Furthermore, the misalignment of band energy also leads to the accumulation of photogenerated charges that could make against the charge extraction.[32] The more suited the valence band between $MAPbI_3$ and HTL is, the easier holes are extracted. Moreover, the amount of holes transferred to HTL is increased. Therefore, the hole extraction and transfer are enhanced after MLG modified the NiO_x layer. It can be expected that the Voc of the device based on NiO_x/MLG will be higher than that on NiO_x.

2.1.3. Device Architecture and Photovoltaic Performance

Figure 5a shows the device architecture that consists of FTO-glass, hole transport layer (MLG modified NiO_x), perovskite layer ($MAPbI_3$), electron transport layer (PCBM), interfacial layer (BCP), and contact (Ag). Given that the NiO_x is prepared via a low-temperature process, defects exist in the film inevitably. Worse, the defects usually cause the poor interface contact between NiO_x film and $MAPbI_3$ layer, leading to poor crystallinity and morphology of $MAPbI_3$ and even the low light absorption and charge recombination. Therefore, the insertion of MLG in the interface between NiO_x film and $MAPbI_3$ layer can shield the defects in NiO_x film, overcoming the above-mentioned obstacles to obtain a high-quality $MAPbI_3$ layer. Figure 5b displays the mechanism of MLG shielding the defects in NiO_x film.

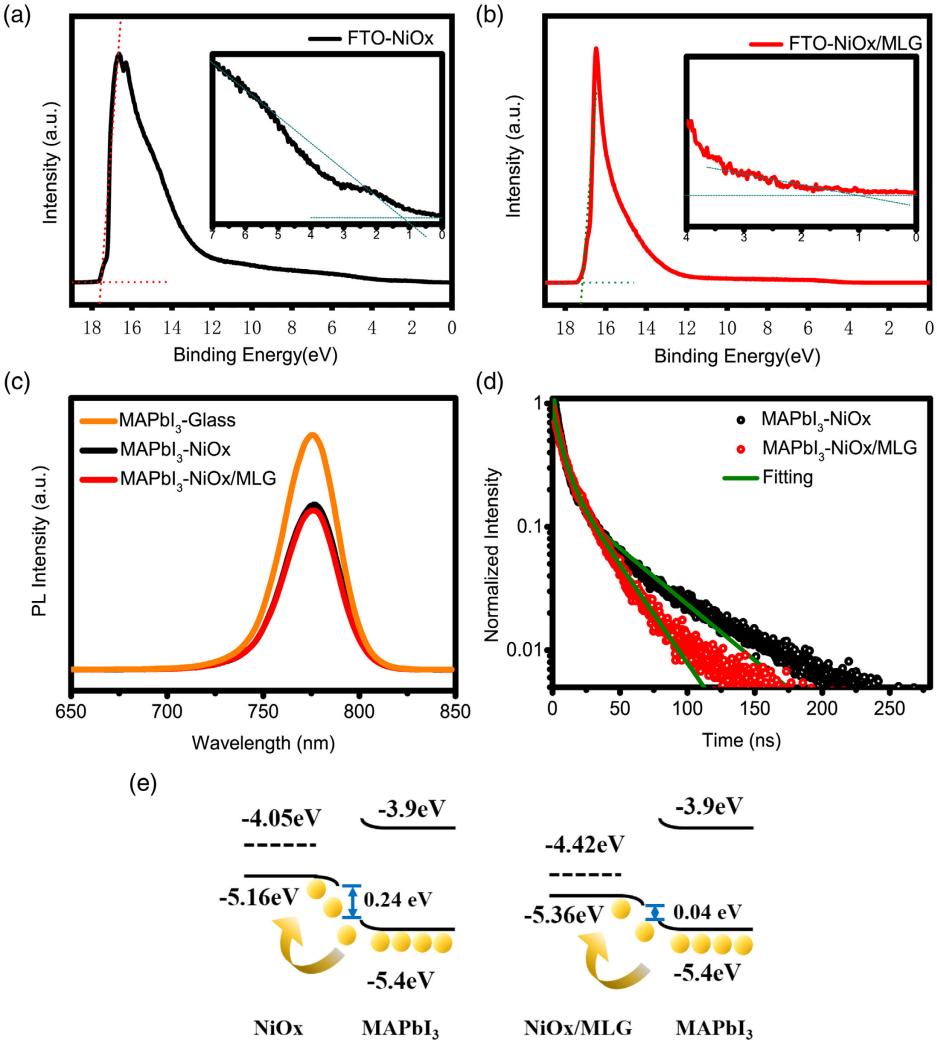

Figure 4. Ultraviolet photoelectron spectroscopy (UPS) spectra of: a) NiO_x and b) NiO_x/MLG on FTO; c) Steady-state photoluminescence (PL) spectra of $MAPbI_3$ films on glass, NiO_x, and NiO_x/MLG; d) time-resolved PL (TRPL) spectra of $MAPbI_3$ on NiO_x and NiO_x/MLG; e) Schematic diagram of hole transportation at the interface between NiO_x (left), NiO_x/MLG (right) and $MAPbI_3$ film under illumination.

The energy level of every layer is summarized in Figure 5c, in which the energy level of NiO_x and NiO_x/MLG is calculated from UPS shown earlier, and of the other layers (FTO, $MAPbI_3$, PCBM, BCP, and Ag) refers to the published works.[33] It is distinctly illustrated that the valence band of NiO_x/MLG is closer to it of $MAPbI_3$ than that of NiO_x, which is conductive to hole extraction. The cross-sectional SEM images of devices based on NiO_x and NiO_x/MLG are compared in Figure 5d,e, distinguished hierarchical in the device. In the meanwhile, the cross-sectional SEM images also agree with the morphology SEM result that the $MAPbI_3$ on NiO_x/MLG displays larger grains.

Additionally, as another measure of $MAPbI_3$ film quality, trap-state density (n_{trap}) can be calculated quantitatively by the space charge-limited current (SCLC) technique. As the modification of MLG is located between the hole transport layer and $MAPbI_3$, the hole n_{trap} would be affected. The dark J-V curves of the hole-only devices based on NiO_x and NiO_x/MLG are measured and fitted in **Figure 6**a,b, with the structure of FTO/NiO_x/(MLG/) perovskite/spiro-OMeTAD/Ag. According to the dependence of current on the applied voltage, the plot can be divided into three regions 1) the ohmic region at low bias showing a linear relationship between the current and the electric field; 2) the child region at high bias; 3) trap-filling limit (TFL) region exhibiting a sharp increase in the current. In the TFL region, traps are filled until trap-filling limit voltage (V_{TFL}) as bias increases,[34] in which n_{trap} can be calculated by Equation (1)

$$n_{trap} = \frac{2\varepsilon\varepsilon_0 V_{TFL}}{eL^2} \tag{1}$$

where e is the elementary charge (1.6×10^{-14} C), L is the thickness of the perovskite layer (455 nm from the cross-sectional SEM), ε_0 is the vacuum permittivity ($\approx 8.85 \times 10^{-14}$ F cm^{-1}), ε is the relative dielectric constant of the perovskite layer (adopt at $\approx$28.8). The V_{TFL} value for the device base on NiO_x and NiO_x/MLG is 0.794 and 0.494 V, respectively. The calculated

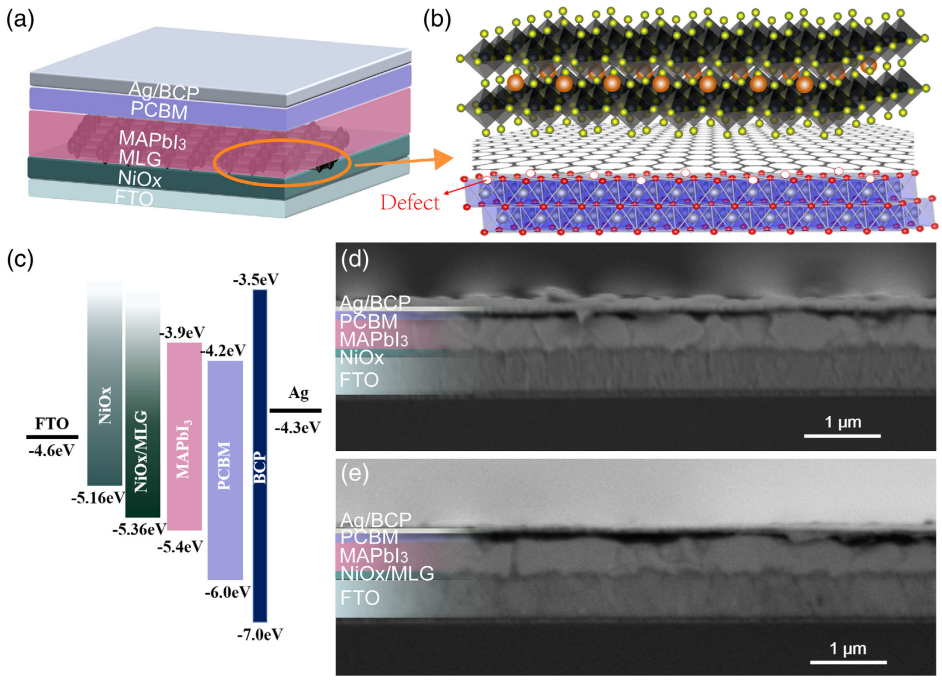

Figure 5. a) Schematic illustration of the inverted perovskite solar cell (PSC) based on MLG; b) Schematic diagram of MLG inserting the interface between NiO_x film and $MAPbI_3$ layer; c) Energy level diagram of each layer in the device; Cross-sectional SEM image of the real device based on d) NiO_x and e) NiO_x/MLG.

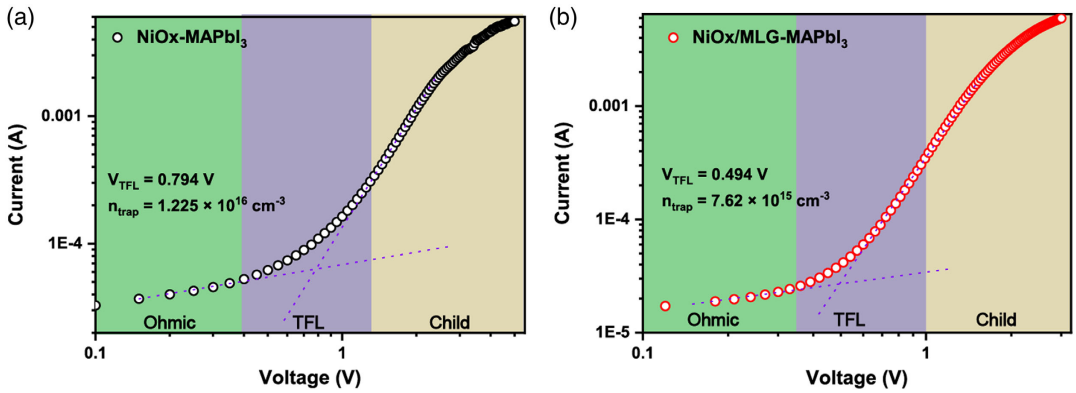

Figure 6. Space charge-limited current (SCLC) versus voltage of hole-only device based on: a) NiO_x-$MAPbI_3$ and b) NiO_x/MLG-$MAPbI_3$.

hole n_{trap} for the device base on NiO_x/MLG is $7.62 \times 10^{15}\,cm^{-3}$, which is much lower than that based on NiO_x ($1.225 \times 10^{16}\,cm^{-3}$). Therefore, the SCLC result agrees with the aforementioned result that the quality of $MAPbI_3$ is enhanced after introducing MLG between NiO_x and $MAPbI_3$.

Photovoltaic performance is the most important and intuitive evaluation criterion for PSCs. We analyze the photovoltaic performance of the device based on NiO_x and NiO_x/MLG comprehensively and present it in **Figure 7**. For inverted PSCs, hysteresis behavior is known to be negligible. The J–V curves of the champion devices based on NiO_x and NiO_x/MLG HTL are exhibited in Figure 7a,b. Both devices based on NiO_x and NiO_x/MLG show negative hysteresis, which also demonstrates the good carrier transport at every layer. It is demonstrated that the photovoltaic performance is remarkably boosted after using MLG modifying NiO_x HTL. The photovoltaic parameters from J–V curves for both devices are listed inset in Figure 7a. The champion device based on NiO_x obtains a PCE of 18.35%. While with the modification of MLG, the device PCE reaches 19.21%. By comparison, the improvement of photovoltaic parameters mainly comes from the enhancement of V_{oc}, attributed to the alignment of energy levels. The detailed statistical photovoltaic parameters of PSCs based on NiO_x and NiO_x/MLG are compared and listed in Figure 7c, which summarized the photovoltaic parameters of devices in Table S2 and S3, Supporting Information. It is obviously shown that the parameters are enhanced with the modification of MLG, and distributed in

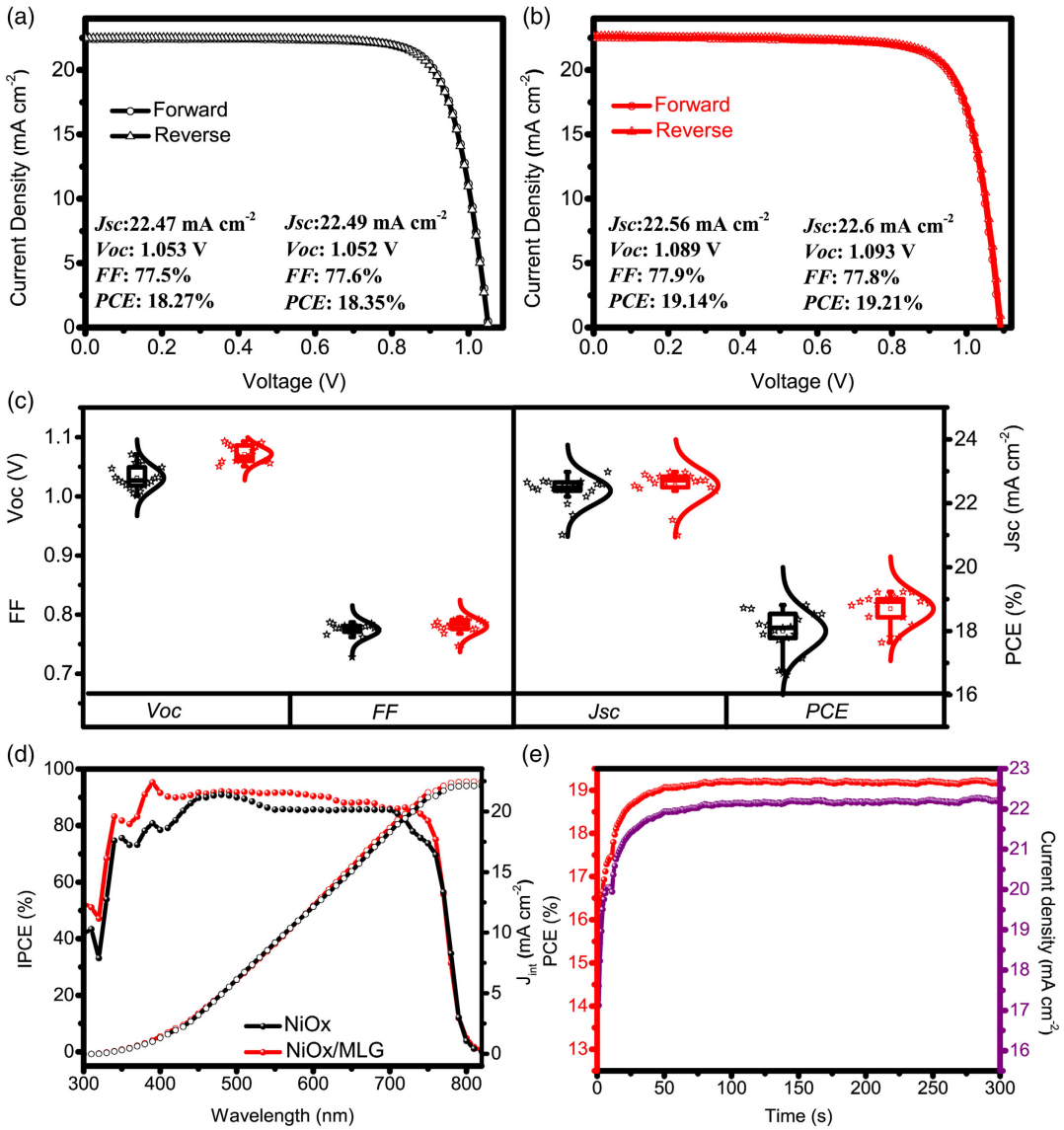

Figure 7. Hysteresis characteristics of the corresponding champion devices based on: a) NiO_x and b) NiO_x/MLG; c) Statistics of photovoltaic statistic parameters from the devices based on NiO_x and NiO_x/MLG; d) incident photon-current conversion efficiency (IPCE) spectra and e) stabilized power output curves of the champion device based on NiO_x/MLG.

a narrow range, suggesting excellent reproducibility. The improvements of both V_{oc} and *FF* mean the MLG modification of NiO_x decreases the recombination effectively at the NiO_x–$MAPbI_3$ interface and the enhancement of carrier transport. Moreover, the incident photon-current conversion efficiency (IPCE) is carried out to study the photon to current conversion efficiency and integrate the current density of both devices based on NiO_x and NiO_x/MLG. As shown in Figure 7d, both the devices display the charge collection over the broad spectral range from 350-800 nm with average efficiency of over 85%. As expected, the NiO_x/MLG-based device shows higher IPCE, which is probably on account of the enhanced charge transfer and balanced photocurrent collection.[35] The integrated photocurrent densities for each device are 22.47 and 22.13 mA cm^{-2}, respectively, which are slightly lower than those attained from *J*–*V* curves. Given that the IPCE measurements are carried out without one-sun illumination, the integrated current densities from IPCE curves are usually lower than that obtained from *J*–*V* curves.[36] Finally, stabilized power output test for the device based on NiO_x/MLG is carried out by holding the voltage at the maximum power point as long as 300 s ($V_{max} = 0.9138$ V), which is shown in Figure 7e. The stabilized PCE and J_{sc} constantly stay along the time at about 19.18%, and 22.27 mA cm^{-2}, which are comparable to the PCE and J_{sc} obtained from *J*–*V* curves of a device based on NiO_x/MLG. In the meanwhile, the results of stabilized power output test for the device based on NiO_x are shown in Figure S2, Supporting Information.

3. Conclusion

In summary, MLG was used for NiO_x/perovskite interface modification. After modification, a 0.1 eV drop of the HOMO level was obtained. Perovskite layer with high crystallinity and large grain was made on the NiO_x/adenine substrate. Improved contact, accelerated charge transport, and extraction were achieved in the HTL/perovskite interface after adenine modification. Compared with the control NiO_x device, an enhancement of Voc and Jsc was observed after adenine modification. Moreover, a significant improvement in device stability was achieved in adenine-modified devices. Therefore, this work provides a novel interface engineering strategy between NiO_x and perovskites, which is helpful for minimizing the voltage deficit and improving PSC stability.

4. Experimental Section

Materials: Unless otherwise indicated, all materials were used as received and purchased from Sigma-Aldrich. $MAPbI_3$ film was fabricated using PbI_2:MAI(1:1)-dimethylformamide complex (99.99%, TCI) and dimethylsulfoxide (DMSO) solvent from Acros Organics.

Fabrication of Crack-Free Monolayer Graphene: First, the crack-free MLG was deposited on Cu foil by the CVD method, according to our previous article.[24] The Cu foil was annealed at 1000 °C under a CO_2 atmosphere to clean the surface, and after eliminating the CO_2, CH_4 was added to deposit MLG. Next, PMMA with a thickness of 100–200 nm was coated on the exposed surface of MLG to reinforce the mechanical strength. Following, the Cu foil was etched in a 0.2 M $Na_2S_2O_8$ aqueous solution, leaving the PMMA-coated MLG film floating on the aqueous solution. Subsequently, the floating PMMA/MLG film was salvaged on the surface of the FTO-NiO_x substrate. Finally, the PMMA was removed by dissolving in acetone to expose the clean MLG surface.

Fabrication of Perovskite Solar Cells: FTO glass substrates (Nippon sheet glass) were sequentially cleaned with the detergent solution, acetone, and ethanol in an ultrasonic bath. After UV-O_3 treatment, NiO_x thin layer was loaded on FTO glass by spin-coating at 4000 rpm for 30 s with 20 mg mL^{-1} NiO_x aqueous dispersion and dried at 150 °C for 10 min. Here, the 20 mg mL^{-1} NiO_x aqueous dispersion was fabricated as our reported article. First, 10 M NaOH solution was dropped-wise into 0.5 M $NiCl_2{\cdot}6H_2O$ solution until the pH value reached 10. Then, the obtained green precipitation was centrifuged, washed three times with deionized water, and dried at 80 °C overnight. After being ground, the green powder was annealed at 270 °C for 2 h to obtain NiO_x nanoparticles. The NiO_x nanoparticles were dispersed in deionized water by ultrasound for the concentration of 20 mg mL^{-1}. Before use, it was filtrated with a 0.45 μm polytetrafluoroethylene (PTFE) filter.

The large-area crack-free MLG was coated on NiO_x film as the aforementioned method, which was then treated in UV-O_3 for 10 min to improve the surface wettability. For 1.8 M $MAPbI_3$ precursor solution, the $MAPbI_3$ single crystal was dissolved in DMSO solution, which was spin-coated on the substrates at 1000 rpm for 10 s and continuously at 4000 rpm for 30 s. During the second step, 600 μL of chlorobenzene was poured at the 20 s to rush the film for extracting the DMSO. The $MAPbI_3$ films were crystallized on a hot plate at 100 °C for 1 h. After cooling down, 20 mg mL^{-1} PCB61M solution was spin-coated at 1500 rpm for 30 s as an electron transfer layer. Following, saturated bathocuproine (BCP) isopropanol solution was spin-coated on PC61BM film at 6000 rpm for 30 s. Finally, silver top electrodes with a thickness of 100 nm were thermal evaporated to complete finish the fabrication of the PSCs.

Characterization: XRD measurement was carried out using a Bruker D8 Advance diffractometer in an angle range of $2\theta = 10°$ to 70°. The morphology was characterized using an SEM (ZEISS Merlin) and atomic force microscope (AFM, Bruker). Raman characterization was carried out using a Renishaw micro-Raman spectroscope (532 nm, 2.33 eV, ×100 objective) and analyzed by MATLAB. Absorbance and transmittance spectra of NiO_x and NiO_x/MLG films on FTO were measured with an integrating sphere using UV/Vis/NIR spectroscopy (PerkinElmer Lambda). UPS were taken on an AXIS SUPRA instrument (Kratos Analytical). PL dynamics were measured using time-resolved single photon counting (TRSPC), which is incorporated into the Fluorolog-312 spectrofluorometer. The SCLC plots were obtained using a digital source meter (Keithley 2400). The current density–voltage (*J*–*V*) characteristics of the solar cells were measured using Keithley 2400 under AM 1.5G irradiation (100 mW cm^{-2}) from commercial solar simulators (Oriel, 450 W Xenon, AAA class). The light intensity was calibrated with a Si reference cell equipped with an IR-cutoff filter (KG5, Newport). The voltage scan rate was 10 or 25 mV s^{-1}. The active area of solar cells is 0.16 cm^2 by a mask to fix the effective area and reduce the influence of the scattered light. Before measurement, there was no preconditioning such as light soaking or forward voltage bias. External quantum efficiency (EQE) was measured by IQE200B (Oriel) without bias light.

Supporting Information

Supporting Information is available from the Wiley Online Library or from the author.

Acknowledgements

The authors acknowledge the National Natural Science Foundation of China (Nos. U1732126, 52072182, and 51872145), the China Postdoctoral Science Foundation (Nos. 2019M650120 and 2020M671554), and the National Synergetic Innovation Center for Advanced Materials (SICAM). S.H. and K.V.A. acknowledge GAZNAT. The authors extend their appreciation to the Deputyship for Research & Innovation, Ministry of Education in Saudi Arabia, for funding this research work through project number 526.

Conflict of Interest

The authors declare no conflict of interest.

Data Availability Statement

The data that support the findings of this study are available in the supplementary material of this article.

Keywords

hole transport layers, monolayer graphene, NiO_x, perovskite solar cells

Received: May 26, 2022
Published online:

[1] T. Zhu, L. Shen, S. Xun, J. S. Sarmiento, Y. Yang, L. Zheng, H. Li, H. Wang, J. L. Bredas, X. Gong, *Adv. Mater.* **2022**, *34*, e2109348.
[2] J. J. Yoo, G. Seo, M. R. Chua, T. G. Park, Y. Lu, F. Rotermund, Y. K. Kim, C. S. Moon, N. J. Jeon, J. P. Correa-Baena, V. Bulovic, S. S. Shin, M. G. Bawendi, J. Seo, *Nature* **2021**, *590*, 587.
[3] M. Kim, J. Jeong, H. Lu, T. K. Lee, F. T. Eickemeyer, Y. Liu, I. W. Choi, S. J. Choi, Y. Jo, H.-B. Kim, S.-I. Mo, Y.-K. Kim, H. Lee, N. G. An, S. Cho, W. R. Tress, S. M. Zakeeruddin, A. Hagfeldt, J. Y. Kim, M. Gratzel, D. S. Kim, *Science* **2022**, *375*, 302.
[4] F. Yu, J. Liu, J. Huang, P. Xu, C.-H. Li, Y.-X. Zheng, H. Tan, J.-L. Zuo, *Sol. RRL* **2021**, *6*, 2100906.

[5] R. Hu, L. Chu, J. Zhang, X. A. Li, W. Huang, *J. Power Sources* **2017**, *361*, 259.
[6] H. Min, D. Y. Lee, J. Kim, G. Kim, K. S. Lee, J. Kim, M. J. Paik, Y. K. Kim, K. S. Kim, M. G. Kim, T. J. Shin, I. S. Seok, *Nature* **2021**, *598*, 444.
[7] D. Yang, X. Zhang, K. Wang, C. Wu, R. Yang, Y. Hou, Y. Jiang, S. Liu, S. Priya, *Nano Lett.* **2019**, *19*, 3313.
[8] F. Li, X. Deng, F. Qi, Z. Li, D. Liu, D. Shen, M. Qin, S. Wu, F. Lin, S. H. Jang, J. Zhang, X. Lu, D. Lei, C. S. Lee, Z. Zhu, A. K. Jen, *J. Am. Chem. Soc.* **2020**, *142*, 20134.
[9] M. Degani, Q. An, M. Albaladejo-Siguan, Y. J. Hofstetter, C. Cho, F. Paulus, G. Grancini, Y. Vaynzof, *Sci. Adv.* **2021**, *7*, eabj7930.
[10] Y. M. Chang, C. W. Li, Y. L. Lu, M. S. Wu, H. Li, Y. S. Lin, C. W. Lu, C. P. Chen, Y. J. Chang, *ACS Appl. Mater. Interfaces* **2021**, *13*, 6450.
[11] S. Wang, Y. Li, J. Yang, T. Wang, B. Yang, Q. Cao, X. Pu, L. Etgar, J. Han, J. Zhao, X. Li, A. Hagfeldt, *Angew. Chem., Int. Ed.* **2022**, e202116534.
[12] J. Zhang, J. Yang, R. Dai, W. Sheng, Y. Su, Y. Zhong, X. Li, L. Tan, Y. Chen, *Adv. Energy Mater.* **2022**, *12*, 2103674.
[13] N. Tiwari, H. Arianita Dewi, E. Erdenebileg, R. Narayan Chauhan, N. Mathews, S. Mhaisalkar, A. Bruno, *Sol. RRL* **2021**, *6*, 2100700.
[14] F. Ma, Y. Zhao, J. Li, X. Zhang, H. Gu, J. You, *J. Energy Chem.* **2021**, *52*, 393.
[15] S. Teo, Z. Guo, Z. Xu, C. Zhang, Y. Kamata, S. Hayase, T. Ma, *ChemSusChem* **2019**, *12*, 518.
[16] Y. Du, C. Xin, W. Huang, B. Shi, Y. Ding, C. Wei, Y. Zhao, Y. Li, X. Zhang, *ACS Sustainable Chem. Eng.* **2018**, *6*, 16806.
[17] W. Chen, Y. Zhou, L. Wang, Y. Wu, B. Tu, B. Yu, F. Liu, H. W. Tam, G. Wang, A. B. Djurisic, L. Huang, Z. He, *Adv. Mater.* **2018**, *30*, e1800515.
[18] Q. Wang, C. C. Chueh, T. Zhao, J. Cheng, M. Eslamian, W. C. H. Choy, A. K. Jen, *ChemSusChem* **2017**, *10*, 3794.
[19] H. Su, T. Wu, D. Cui, X. Lin, X. Luo, Y. Wang, L. Han, *Small Methods* **2020**, *4*, 2000507.
[20] K. Gong, J. Hu, N. Cui, Y. Xue, L. Li, G. Long, S. Lin, *Mater. Des.* **2021**, *211*, 110170.
[21] K. Chung, K. Lee, Y. Tchoe, H. Oh, J. Park, J. K. Hyun, G.-C. Yi, *Nano Energy* **2019**, *60*, 82.
[22] T. Gatti, F. Lamberti, P. Topolovsek, M. Abdu-Aguye, R. Sorrentino, L. Perino, M. Salerno, L. Girardi, C. Marega, G. A. Rizzi, M. A. Loi, A. Petrozza, E. Menna, *Sol. RRL* **2018**, *2*, 1800013.
[23] J. Zhang, J. Fan, B. Cheng, J. Yu, W. Ho, *Sol. RRL* **2020**, *4*, 2000502.
[24] S. Huang, M. Dakhchoune, W. Luo, E. Oveisi, G. He, M. Rezaei, J. Zhao, D. T. L. Alexander, A. Zuttel, M. S. Strano, K. V. Agrawal, *Nat. Commun.* **2018**, *9*, 2632.
[25] C. Klein, D. Cohen-Elias, G. Sarusi, *Heliyon* **2018**, *4*, e01030.
[26] N. Mironova-Ulmane, A. Kuzmin, I. Steins, J. Grabis, I. Sildos, M. Pärs, *J. Phys.: Conf. Ser.* **2007**, *93*, 012039.
[27] X. Xia, Y. Jiang, Q. Wan, X. Wang, L. Wang, F. Li, *ACS Appl. Mater. Interfaces* **2018**, *10*, 44501.
[28] R. Hu, R. Zhang, Y. Ma, W. Liu, L. Chu, W. Mao, J. Zhang, J. Yang, Y. Pu, X. A. Li, *Appl. Surf. Sci.* **2018**, *462*, 840.
[29] R. Hu, C. Ge, L. Chu, Y. Feng, S. Xiao, Y. Ma, W. Liu, X. A. Li, M. K. Nazeeruddin, *J. Energy Chem.* **2021**, *59*, 581.
[30] X. Gong, Q. Sun, S. Liu, P. Liao, Y. Shen, C. Gratzel, S. M. Zakeeruddin, M. Gratzel, M. Wang, *Nano Lett.* **2018**, *18*, 3969.
[31] Q. Jiang, L. Zhang, H. Wang, X. Yang, J. Meng, H. Liu, Z. Yin, J. Wu, X. Zhang, J. You, *Nat. Energy* **2016**, *2*, 1.
[32] M. Stolterfoht, P. Caprioglio, C. M. Wolff, J. Márquez, J. Nordmann, S. Zhang, D. Rothhardt, U. Hrmann, Y. Amir, A. J. E. Redinger, E. Science, *Energy Environ. Sci.* **2019**, *12*, 2778.
[33] Z. Zhou, X. Li, M. Cai, F. Xie, Y. Wu, Z. Lan, X. Yang, Y. Qiang, A. Islam, L. Han, *Adv. Energy Mater.* **2017**, *7*, 1700763.
[34] R. Hu, Y. Zhang, S. Paek, X.-X. Gao, X. A. Li, M. K. Nazeeruddin, *J. Mater. Chem. A* **2020**, *8*, 8058.
[35] W. S. Yang, B. W. Park, E. H. Jung, N. J. Jeon, Y. C. Kim, D. U. Lee, S. S. Shin, J. Seo, E. K. Kim, J. H. J. S. Noh, *Science* **2017**, *356*, 1376.
[36] W. Chen, L. Xu, X. Feng, J. Jie, Z. He, *Adv. Mater.* **2017**, *29*, 1603923.